

J0811+4730: the most metal-poor star-forming dwarf galaxy known

Y. I. Izotov¹, T. X. Thuan², N. G. Guseva¹ and S. E. Liss²

¹*Main Astronomical Observatory, Ukrainian National Academy of Sciences, Zabolotnoho 27, Kyiv 03143, Ukraine, izotov@mao.kiev.ua, guseva@mao.kiev.ua*

²*Astronomy Department, University of Virginia, P.O. Box 400325, Charlottesville, VA 22904-4325, txt@virginia.edu, sel7pa@virginia.edu*

19 October 2018

ABSTRACT

We report the discovery of the most metal-poor dwarf star-forming galaxy (SFG) known to date, J0811+4730. This galaxy, at a redshift $z=0.04444$, has a Sloan Digital Sky Survey (SDSS) g -band absolute magnitude $M_g = -15.41$ mag. It was selected by inspecting the spectroscopic data base in the Data Release 13 (DR13) of the SDSS. LBT/MODS spectroscopic observations reveal its oxygen abundance to be $12 + \log \text{O}/\text{H} = 6.98 \pm 0.02$, the lowest ever observed for a SFG. J0811+4730 strongly deviates from the main-sequence defined by SFGs in the emission-line diagnostic diagrams and the metallicity – luminosity diagram. These differences are caused mainly by the extremely low oxygen abundance in J0811+4730, which is ~ 10 times lower than that in main-sequence SFGs with similar luminosities. By fitting the spectral energy distributions of the SDSS and LBT spectra, we derive a stellar mass of $M_\star = 10^{6.24} - 10^{6.29} M_\odot$ (statistical uncertainties only), and we find that a considerable fraction of the galaxy stellar mass was formed during the most recent burst of star formation.

Key words: galaxies: dwarf – galaxies: starburst – galaxies: ISM – galaxies: abundances.

1 INTRODUCTION

Extremely metal-deficient star-forming galaxies (SFGs) with oxygen abundances $12 + \log \text{O}/\text{H} \lesssim 7.3$ constitute a rare but important class of galaxies in the nearby Universe. They are thought to be the best local analogs of the numerous population of the dwarf galaxies at high redshifts that played an important role in the reionization of the Universe at redshifts $z \sim 5-10$ (e.g. Ouchi et al. 2009; Karman et al. 2017). Their proximity permits studies of their stellar, gas and dust content with a sensitivity and spectral resolution that are not possible for high- z galaxies.

Many efforts have been made in the past to discover the most metal-poor nearby galaxies. The galaxy I Zw 18, first spectroscopically observed by Searle & Sargent (1972), with oxygen abundances $12 + \log \text{O}/\text{H} \sim 7.17-7.26$ in its two brightest regions (e.g. Skillman & Kennicutt 1993; Izotov & Thuan 1998) stood as the lowest-metallicity SFG for a long period. It was replaced by SBS 0335–052W with an oxygen abundance $12 + \log \text{O}/\text{H} = 7.12 \pm 0.03$, derived from the emission of the entire galaxy (Izotov et al. 2005), and oxygen abundances in its two brightest knots of star formation of 7.22 and 7.01 (Izotov et al. 2009).

The large data base of the Sloan Digital Sky Sur-

vey (SDSS) offered a possibility for a systematic search of the most metal-deficient SFGs. In particular, Izotov et al. (2012) and Guseva et al. (2017) found two dozens of galaxies with $12 + \log \text{O}/\text{H} < 7.35$ in the SDSS. However, no SFG with a metallicity below that of SBS 0335–052W was found.

Local galaxies with very low-metallicities have also been discovered in other contexts. Pustilnik, Kniazev & Pramskij (2005) studying the properties of dwarf galaxies in the Cancer-Lynx void found that the weighted mean oxygen abundance in five regions of the irregular dwarf galaxy DDO 68 is $12 + \log \text{O}/\text{H} = 7.21 \pm 0.03$.

Two extremely metal-poor dwarf galaxies were discovered in the course of the Arecibo Legacy Fast ALFA survey (ALFALFA, Giovanelli et al. 2005; Haynes et al. 2011). Skillman et al. (2013) found that the oxygen abundance in the nearby dwarf galaxy AGC 208583 = Leo P is 7.17 ± 0.04 , still more metal-rich than SBS 0335–052W. Finally, Hirschauer et al. (2016) showed that the nearby dwarf galaxy AGC 198691 has an oxygen abundance of $12 + \log \text{O}/\text{H} = 7.02 \pm 0.03$, lower than the average value in SBS 0335–052W.

In this paper, we present Large Binocular Telescope

Table 1. Observed characteristics of J0811+4730

Parameter	Value
R.A.(J2000)	08:11:52.12
Dec.(J2000)	+47:30:26.24
z	0.04444 ± 0.00003
g , mag	21.37 ± 0.05
M_g , mag [†]	-15.41 ± 0.06
$\log M_*/M_\odot$ [‡]	6.24 ± 0.33
$\log M_*/M_\odot$ ^{‡‡}	6.29 ± 0.06
$L(\text{H}\beta)$, erg s ^{-1*}	$(2.1 \pm 0.1) \times 10^{40}$
SFR, M _⊙ yr ^{-1††}	0.48 ± 0.02

[†]Corrected for Milky Way extinction.

[‡]Derived from the extinction- and aperture-corrected SDSS spectrum.

^{‡‡}Derived from the extinction- and aperture-corrected LBT spectrum.

*Corrected for extinction and the SDSS spectroscopic aperture.

^{††}Derived from the Kennicutt (1998) relation using the extinction- and aperture-corrected H β luminosity.

(LBT)¹ spectroscopic observations with high signal-to-noise ratio of the compact dwarf SFG J0811+4730. This galaxy stood out by its emission-line ratios, during the inspection of the spectra in the SDSS Data Release 13 (DR13) data base (Albaret et al. 2016), as potentially having a very low metallicity. Its coordinates, redshift and other characteristics obtained from the SDSS photometric and spectroscopic data bases are shown in Table 1.

The LBT observations and data reduction are described in Sect. 2. We derive element abundances in Sect. 3. Integrated characteristics of J0811+4730 are discussed in Sect. 4. Emission-line diagnostic diagrams and the metallicity-luminosity relation for a sample of the most-metal poor SFGs, including J0811+4730, are considered in Sect. 5. Finally, in Sect. 6 we summarize our main results.

2 LBT OBSERVATIONS AND DATA REDUCTION

We have obtained LBT long-slit spectrophotometric observations of J0811+4730 on 1 February, 2017 in the twin binocular mode using both the MODS1 and MODS2 spectrographs², equipped with two 8022 pix \times 3088 pix CCDs. The G400L grating in the blue beam, with a dispersion of 0.5Å/pix, and the G670L grating in the red beam, with a dispersion of 0.8Å/pix, were used. Spectra were obtained in

the wavelength range 3200 – 10000Å with a 1.2 arcsec wide slit, resulting in a resolving power $R \sim 2000$. The seeing during the observations was in the range 0.5 – 0.6 arcsec.

Six 890 s subexposures were obtained with each spectrograph, resulting in the total exposure of 2×5340 s counting both spectrographs. The airmass varied from 1.16 for the first subexposure to 1.05 for the sixth subexposure. The slit was oriented at the fixed position angle of 80°. This is to be compared with the parallactic angles of 74° during the first subexposure and of 53° during the sixth subexposure. According to Filippenko (1982), such differences between the position angle and the parallactic angle would result in an offset perpendicular to the slit of the [O II] $\lambda 3727$ wavelength region relative to the H β wavelength region of less than 0.1 – 0.2 arcsec. Thus, the effect of atmospheric refraction is small for all subexposures.

The spectrum of the spectrophotometric standard star GD 71, obtained during the same night with a 5 arcsec wide slit, was used for flux calibration. It was also used to correct the red part of the J0811+4730 spectrum for telluric absorption lines. Additionally, calibration frames of biases, flats and comparison lamps were obtained during the daytime, after the observations.

The MODS Basic CCD Reduction package MODSCC-DRED³ was used for bias subtraction and flat field correction, while wavelength and flux calibration was done with IRAF⁴. Finally, all MODS1 and MODS2 subexposures were combined. The one-dimensional spectrum of J0811+4730 shown in Fig. 1 was extracted in a 1.2 arcsec aperture along the spatial axis. Strong emission lines are present in this spectrum, suggesting active star formation. In particular, a strong [O III] $\lambda 4363$ emission line is detected, allowing a reliable abundance determination. Because of the importance of this line, we have checked whether its flux can be affected by such events as cosmic ray hits. We find that the flux ratio of [O III] $\lambda 4363$ to the nearest H γ $\lambda 4340$ emission line is nearly constant in all MODS1 and MODS2 subexposures, varying by not more than 1 – 2 per cent. This implies that the [O III] $\lambda 4363$ emission line is not affected by cosmic ray hits.

Emission-line fluxes were measured using the IRAF SPLOT routine. The errors of the line fluxes were calculated from the photon statistics in the non-flux-calibrated spectra, and by adding a relative error of 1 per cent in the absolute flux distribution of the spectrophotometric standard star. They were then propagated in the calculations of the elemental abundance errors.

The observed fluxes were corrected for extinction, derived from the observed decrement of the hydrogen Balmer emission lines H α , H β , H γ , H δ , H9, H10, H11, and H12. Two lines, H7 and H8, were however excluded because they are blended with other lines. The equivalent widths of the underlying stellar Balmer absorption lines, assumed to be the same for each line, were derived simultaneously with the extinction in an iterative manner, following Izotov et al.

¹ The LBT is an international collaboration among institutions in the United States, Italy and Germany. LBT Corporation partners are: The University of Arizona on behalf of the Arizona university system; Istituto Nazionale di Astrofisica, Italy; LBT Beteiligungsgesellschaft, Germany, representing the Max-Planck Society, the Astrophysical Institute Potsdam, and Heidelberg University; The Ohio State University, and The Research Corporation, on behalf of The University of Notre Dame, University of Minnesota and University of Virginia.

² This paper used data obtained with the MODS spectrographs built with funding from NSF grant AST-9987045 and the NSF Telescope System Instrumentation Program (TSIP), with additional funds from the Ohio Board of Regents and the Ohio State University Office of Research.

³ <http://www.astronomy.ohio-state.edu/MODS/Manuals/MODSCCRed.pdf>

⁴ IRAF is distributed by the National Optical Astronomy Observatories, which are operated by the Association of Universities for Research in Astronomy, Inc., under cooperative agreement with the National Science Foundation.

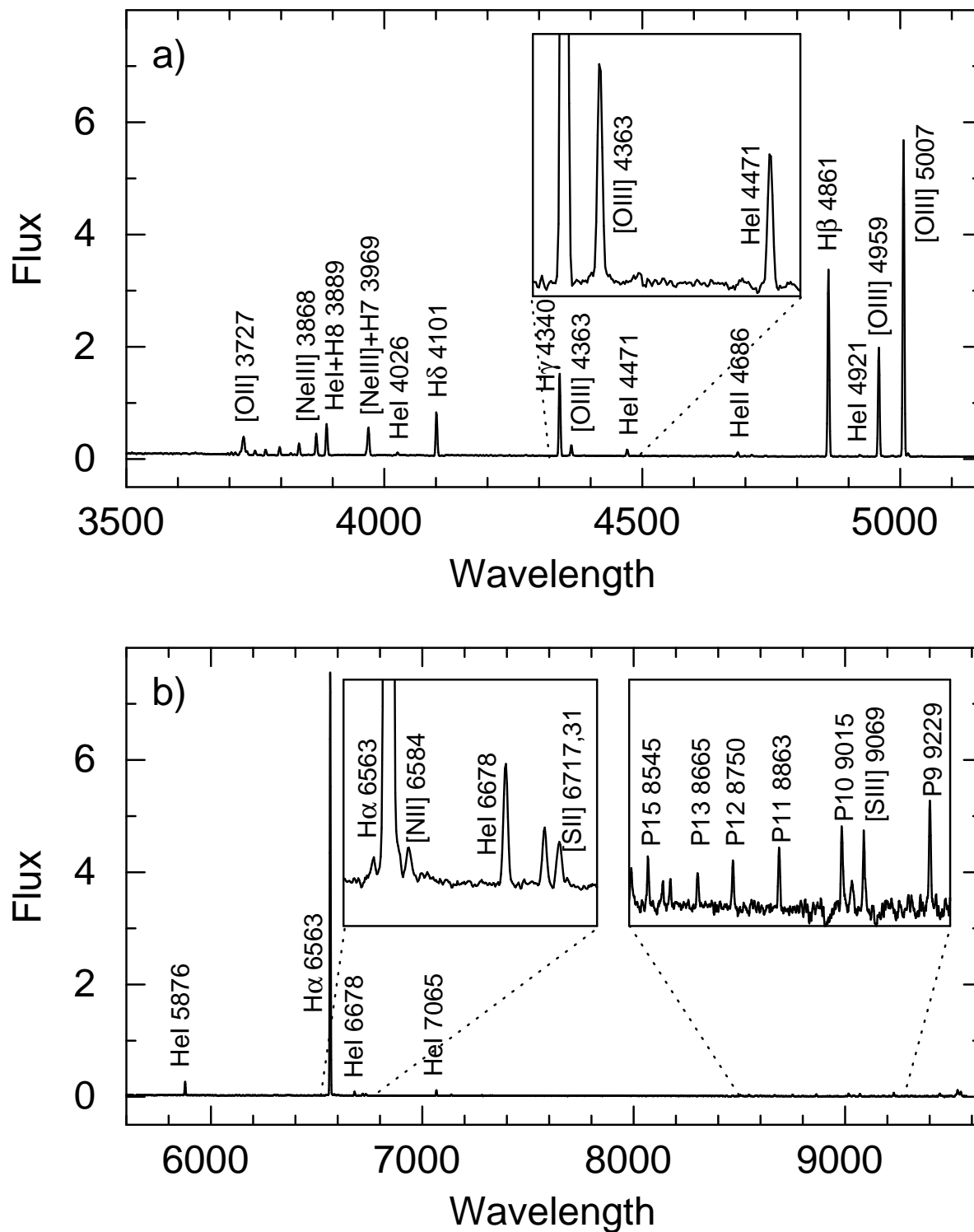


Figure 1. The rest-frame LBT spectrum of J0811+4730 uncorrected for extinction. Insets show expanded parts of spectral regions in the rest wavelength ranges 4320 \AA – 4490 \AA , 6520 \AA – 6770 \AA and 8500 \AA – 9280 \AA for a better view of weak emission lines. Some interesting emission lines are labelled. Wavelengths are in \AA and fluxes are in units of $10^{-16} \text{ erg s}^{-1} \text{ cm}^{-2} \text{ \AA}^{-1}$.

Table 2. Observed and extinction-corrected emission-line fluxes

Line	$100 \times F(\lambda)/F(H\beta)$	$100 \times I(\lambda)/I(H\beta)$
3187.74 He I	2.71±0.66	3.32±0.81
3203.10 He II	1.71±0.89	2.09±1.02
3703.30 H16	1.35±0.14	3.41±0.36
3711.97 H15	1.83±0.20	3.72±0.49
3721.94 H14	2.22±0.18	5.83±0.90
3727.00 [O II]	14.70±0.33	16.75±0.40
3734.37 H13	1.52±0.23	3.61±1.00
3750.15 H12	2.73±0.23	4.73±0.45
3770.63 H11	2.85±0.19	4.89±0.40
3797.90 H10	4.48±0.19	6.66±0.36
3819.64 He I	1.18±0.16	1.33±0.18
3835.39 H9	6.37±0.22	8.86±0.38
3868.76 [Ne III]	11.91±0.28	13.39±0.32
3889.00 He I+H8	17.26±0.34	20.96±0.48
3968.00 [Ne III]+H7	18.05±0.34	21.69±0.47
4026.19 He I	1.59±0.14	1.76±0.15
4068.60 [S II]	0.29±0.09	0.31±0.10
4101.74 H δ	23.26±0.40	26.83±0.51
4120.84 He I	0.39±0.09	0.43±0.10
4340.47 H γ	44.14±0.69	48.13±0.80
4363.21 [O III]	5.93±0.19	6.26±0.20
4387.93 He I	0.18±0.09	0.18±0.09
4471.48 He I	3.51±0.15	3.65±0.16
4658.10 [Fe III]	0.51±0.10	0.52±0.10
4685.94 He II	2.24±0.15	2.27±0.15
4712.00 [Ar IV]+He I	0.91±0.16	0.91±0.16
4740.20 [Ar IV]	0.57±0.11	0.58±0.11
4861.33 H β	100.00±1.50	100.00±1.52
4921.93 He I	0.97±0.13	0.95±0.13
4958.92 [O III]	56.75±0.88	55.60±0.87
4988.00 [Fe III]	0.44±0.09	0.43±0.09
5006.80 [O III]	165.79±2.46	161.59±2.42
5015.68 He I	1.91±0.13	1.86±0.13
5875.60 He I	10.38±0.18	9.45±0.17
6300.30 [O I]	0.65±0.06	0.60±0.05
6312.10 [S III]	0.46±0.06	0.41±0.06
6548.10 [N II]	0.38±0.02	0.33±0.02
6562.80 H α	311.93±4.56	273.87±4.38
6583.40 [N II]	0.72±0.06	0.63±0.06
6678.10 He I	2.97±0.08	2.59±0.08
6716.40 [S II]	1.39±0.06	1.21±0.05
6730.80 [S II]	1.23±0.06	1.07±0.05
7065.30 He I	3.88±0.09	3.31±0.08
7135.80 [Ar III]	0.99±0.06	0.84±0.05
8545.00 P15	1.31±0.10	1.23±0.10
8665.00 P13	0.99±0.10	0.95±0.10
8750.00 P12	1.23±0.10	1.13±0.10
8863.00 P11	1.70±0.13	1.48±0.11
9015.00 P10	2.43±0.15	2.06±0.13
9069.00 [S III]	2.14±0.18	1.81±0.15
9229.00 P9	2.94±0.20	2.45±0.17
$C(H\beta)^a$	0.165±0.019	
$F(H\beta)^b$	12.60±0.05	
EW(H β) ^c	282.0±1.0	
EW(abs) ^c	2.8±0.3	

^aExtinction coefficient, derived from the observed hydrogen Balmer decrement.

^bObserved flux in units of 10^{-16} erg s⁻¹ cm⁻².

^cEquivalent width in Å.

Table 3. Electron temperatures and element abundances

Property	Value
$T_e(O III)$, K	21700±500
$T_e(O II)$, K	15600±500
$T_e(S III)$, K	19700±500
$N_e(S II)$, cm ⁻³	380±140
$O^+/H^+ \times 10^6$	1.405±0.115
$O^{2+}/H^+ \times 10^6$	7.884±0.398
$O^{3+}/H^+ \times 10^6$	0.244±0.021
$O/H \times 10^6$	9.532±0.415
12+log(O/H)	6.979±0.019
$N^+/H^+ \times 10^7$	0.404±0.053
ICF(N)	6.384
$N/H \times 10^7$	2.785±0.358
log(N/O)	-1.535±0.044
$Ne^{2+}/H^+ \times 10^6$	1.409±0.072
ICF(Ne)	1.073
$Ne/H \times 10^6$	1.512±0.087
log(Ne/O)	-0.800±0.031
$S^+/H^+ \times 10^7$	0.213±0.021
$S^{2+}/H^+ \times 10^7$	0.996±0.146
ICF(S)	1.621
$S/H \times 10^7$	1.961±0.237
log(S/O)	-1.687±0.056
$Ar^{2+}/H^+ \times 10^8$	2.174±0.142
$Ar^{3+}/H^+ \times 10^8$	2.482±0.494
ICF(Ar)	1.223
$Ar/H \times 10^8$	2.659±0.628
log(Ar/O)	-2.555±0.104
$Fe^{2+}/H^+ \times 10^7$	0.898±0.185
ICF(Fe)	9.263
$Fe/H \times 10^7$	8.315±1.716
log(Fe/O)	-1.060±0.092

(1994). They are shown in Table 2. All hydrogen lines were corrected for underlying absorption, in addition to correction for extinction. It is seen from Table 2 that the corrected fluxes of the H9 – H16 emission lines are somewhat larger than the case B values. This is probably due to an over-correction of underlying absorption for these higher order lines. However, this overcorrection makes little difference on the determination of extinction which depends mainly on the observed decrement of the H α , H β , H γ and H δ emission lines.

We note that excluding H α , the only Balmer hydrogen line observed in the red part of the spectrum, in the extinction determination would result in a somewhat higher extinction coefficient, $C(H\beta) = 0.185$ compared to the value of 0.165 in Table 2. This disagreement is small, within the errors. It probably comes from a slight mismatch between the blue and red parts of the spectrum, not exceeding a few per cent of the continuum flux in the overlapping wavelength range. We have adopted the value of 0.165. It is somewhat higher than the $C(H\beta)$ expected for extremely low-metallicity SFGs. However, part of this extinction is due to the Milky Way with relatively high $A(V)_{MW} = 0.180$

mag according to the NASA/IPAC Extragalactic Database (NED) and corresponding to $C(\text{H}\beta)_{\text{MW}}=0.085$. Therefore, the internal extinction coefficient in J0811+4730 is only $C(\text{H}\beta)_{\text{int}}=0.080$. We have adopted the reddening law by Cardelli, Clayton & Mathis (1989) with a total-to-selective extinction ratio $R(V) = 3.1$.

The observed emission-line fluxes $F(\lambda)/F(\text{H}\beta)$ multiplied by 100, the emission-line fluxes corrected for underlying absorption and extinction $I(\lambda)/I(\text{H}\beta)$ multiplied by 100, the extinction coefficient $C(\text{H}\beta)$, the rest-frame equivalent width $\text{EW}(\text{H}\beta)$, the equivalent width of the Balmer absorption lines, and the observed $\text{H}\beta$ flux $F(\text{H}\beta)$ are listed in Table 2. We note that the $\text{EW}(\text{H}\beta)$ in J0811+4730 is high, $\sim 280\text{\AA}$, implying that its optical emission is dominated by radiation from a very young burst, with age ~ 3 Myr.

It is seen in Fig. 1 that the ratio of $\text{H}\alpha$ and $\text{H}\beta$ peak intensities (slightly larger than 2) is lower than the ratio of their total fluxes (about a factor of 3). This is in large part due to the somewhat different spectral resolution of the blue and red spectra of J0811+4730, as they were obtained with different gratings. Indeed, the full widths at half maximum (FWHMs) of $\text{H}\alpha$ and $\text{H}\beta$ are 4.4\AA and 2.9\AA , respectively. These widths are larger than the widths of the Ar lines of 3.6\AA and 2.2\AA in the blue and red comparison spectra, respectively, indicating that both profiles are partially resolved. By deconvolving the instrumental profiles from the observed profiles, we obtain an intrinsic velocity dispersion σ of $\sim 45\pm 5$ km s $^{-1}$ for both the $\text{H}\alpha$ and $\text{H}\beta$ emission lines. This value is separately derived from each of the MODS1 and MODS2 spectra. The uncertainty is derived from the Gaussian fitting of both lines, followed by the deconvolution of their profiles. The velocity dispersion value is fully consistent with the one expected from the $L(\text{H}\beta) - \sigma$ relation for supergiant H II regions (e.g. Chávez et al. 2012), and supports the assumption that the emission lines originate from a single H II region.

3 ELEMENT ABUNDANCES

The procedures described by Izotov et al. (2006) are used to determine element abundances from the LBT spectrum. We note that SDSS spectra of J0811+4730 are available in Data Releases 13 and 14, but they cannot be used for abundance determination because the strong lines are clipped in those spectra. The temperature $T_e(\text{O III})$ is calculated from the $[\text{O III}] \lambda 4363 / (\lambda 4959 + \lambda 5007)$ emission-line flux ratio. It is used to derive the abundances of O^{2+} , Ne^{2+} and Ar^{3+} . To obtain the abundances of O^+ , N^+ , S^+ and Fe^{2+} , the electron temperature $T_e(\text{O II})$ needs to be derived. In principle, this can be done by using the $[\text{O II}] \lambda 3727 / (\lambda 7320 + \lambda 7330)$ flux ratio. However, the latter two lines are extremely weak in the spectrum of J0811+4730, making such a determination of $T_e(\text{O II})$ not possible. Similarly, the electron temperature $T_e(\text{S III})$ is needed to derive the S^{2+} and Ar^{2+} abundances. It can be obtained from the $[\text{S III}] \lambda 6312 / (\lambda 9069 + \lambda 9531)$ flux ratio. However, the $[\text{S III}] \lambda 6312$ line is very weak (Table 2) and the $[\text{S III}] \lambda 9069$ line, at the J0811+4730 redshift, falls at the wavelength of $\sim 9475\text{\AA}$, in a region with numerous night sky emission lines (e.g., fig. 9 in Law et al. 2011) and telluric absorption lines (e.g., fig. 1 in Rudolf et al. 2016). Furthermore, the strongest $[\text{S III}] \lambda 9531$ line is at the very

edge of the LBT spectrum, where the sensitivity is low. All these factors make the determination of $T_e(\text{S III})$ somewhat uncertain. In fact, using the $[\text{S III}] \lambda 6312$ and $[\text{S III}] \lambda 9069$ fluxes from Table 2, equations from Aller (1984) and adopting $[\text{S III}] \lambda 9531 / \lambda 9069 = 2.4$ we derive the high and very uncertain value $T_e(\text{S III}) = 27000 \pm 6000\text{K}$.

Therefore we have used the expressions of Izotov et al. (2006), obtained from photoionized H II region models, to derive the electron temperatures $T_e(\text{O II})$ and $T_e(\text{S III})$. We have also adopted the errors for these temperatures to be equal to the error for the electron temperature $T_e(\text{O III})$. The errors quoted for $T_e(\text{O II})$ and $T_e(\text{S III})$ should be considered as lower limits as they do not take into account the uncertainty introduced by our reliance on grids of photoionization models to determine these temperatures. These models show inevitably a dispersion due to varying parameters such as ionization parameter, electron number density, chemical composition, etc., that will increase the uncertainty in these two temperatures. The electron number density $N_e(\text{S II})$ is derived from the $[\text{S II}] \lambda 6717 / \lambda 6731$ emission line ratio. However, it is not possible to obtain the electron number density from the $[\text{O II}] \lambda 3726 / \lambda 3729$ flux ratio because of the insufficient spectral resolution.

The total oxygen abundance is derived as follows:

$$\frac{\text{O}}{\text{H}} = \frac{\text{O}^+ + \text{O}^{2+} + \text{O}^{3+}}{\text{H}^+}, \quad (1)$$

where the abundances of ions O^+ , O^{2+} , O^{3+} are obtained using the relations of Izotov et al. (2006). For ions of other heavy elements, we also use the relations of Izotov et al. (2006) to derive the ionic abundances, the ionization correction factors and the total heavy element abundances.

The electron temperatures, electron number densities, ionic abundances, ionization correction factors and total heavy element abundances are presented in Table 3. The electron temperature $T_e(\text{O III}) = 21700 \pm 500$ K is derived from the fluxes of $[\text{O III}]$ lines, which were obtained with a high signal-to-noise ratio. The relatively high value of $T_e(\text{O III})$ is a consequence of the very low metallicity of J0811+4730. We note that a temperature of $\gtrsim 20000$ K has been determined in some extremely metal-poor galaxies (e.g. Izotov et al. 2009). CLOUDY models also predict the temperature range 20000 – 23000 K for objects with $12 + \log \text{O}/\text{H} \sim 7.0$, depending on the input parameters.

We derive an oxygen abundance of $12 + \log \text{O}/\text{H} = 6.98 \pm 0.02$, making J0811+4730 the lowest-metallicity SFG known, and the first galaxy with an oxygen abundance below 7.0. We have also derived the oxygen abundance from the MODS1 and MODS2 spectra separately. We obtain respectively $12 + \log \text{O}/\text{H} = 6.98 \pm 0.03$ and 6.97 ± 0.03 , fully consistent with the value obtained from combining all data. If we had adopted the higher extinction coefficient $C(\text{H}\beta) = 0.185$, derived from the hydrogen Balmer decrement by excluding the $\text{H}\alpha$ emission line, we would have obtained an electron temperature higher by 150 K and a slightly lower oxygen abundance, $12 + \log \text{O}/\text{H} = 6.975 \pm 0.019$. The N/O, Ne/O, S/O, Ar/O and Fe/O abundance ratios for this galaxy, shown in Table 3, are similar to those derived for low-metallicity SFGs (e.g., Izotov et al. 2006). We note that the error of the electron temperature $T_e(\text{O II})$ has little impact on the error of $12 + \log \text{O}/\text{H}$. Adopting an error equal to 1500 K instead of 500 K in Table 3 does increase the error

of O^+/H^+ by a factor of 3 but does not change much the error of $12+\log O/H$, increasing it by only 0.005 dex. This is because the O^+ abundance is several times lower than the O^{2+} abundance. The largest impact of such an increased error in $T_e(O II)$ is an increase in the errors of $\log N/O$ and $\log Fe/O$ by ~ 0.03 dex. Similarly, increasing the $T_e(S III)$ error from 500 K to 1500 K would result in increasing the errors in $\log S/O$ and $\log Ar/O$ by ~ 0.03 dex.

4 INTEGRATED CHARACTERISTICS OF J0811+4730

To derive the integrated characteristics of J0811+4730, we adopt the luminosity distance $D = 205$ Mpc. It was obtained from the galaxy redshift with the NED cosmological calculator (Wright 2006), adopting the cosmological parameters $H_0 = 67.1$ km s $^{-1}$ Mpc $^{-1}$, $\Omega_m = 0.318$, $\Omega_\Lambda = 0.682$ (Planck Collaboration XVI 2014) and assuming a flat geometry. The absolute SDSS g magnitude, corrected for the Milky Way extinction $M_g = -15.41$ mag (Table 1), characterizes J0811+4730 as a dwarf SFG.

4.1 $H\beta$ luminosity and star-formation rate

To derive the total $H\beta$ luminosity $L(H\beta)$, we need to correct the observed $H\beta$ flux in the SDSS spectrum for extinction and spectroscopic aperture. Since the strong emission lines in the SDSS spectrum of J0811+4730 are clipped we adopt the extinction coefficient $C(H\beta) = 0.165$ obtained from the observed hydrogen Balmer decrement in the LBT spectrum. The aperture correction is determined as $2.512^{g_{ap}-g}$, where, $g = 21.38 \pm 0.05$ mag and $g_{ap} = 22.28 \pm 0.08$ mag are respectively the SDSS total modelled magnitude and the magnitude inside the spectroscopic aperture of 2 arcsec in diameter. Both quantities, g and g_{ap} , are extracted from the SDSS data base. Using these data we obtain a correction factor of 2.3, which is applied to the $H\beta$ luminosity and some other quantities, such as the stellar mass M_* , obtained from both SDSS and LBT spectra. Here we have assumed that the spatial brightness distributions of the continuum and the hydrogen emission lines are the same. We have checked this assumption by examining the LBT long-slit spectrum. We find from this spectrum that the brightness distributions of $H\beta$, $H\alpha$ and the adjacent continua are indeed nearly identical, with FWHMs of ~ 0.6 arcsec, indicating that the galaxy is mostly unresolved. This angular size corresponds to an upper limit of the galaxy linear size at FWHM of ~ 600 pc.

The star-formation rate (SFR) in J0811+4730, derived from the aperture- and extinction-corrected $H\beta$ luminosity $L(H\beta)$ using the Kennicutt (1998) calibration, is $0.48 M_\odot \text{ yr}^{-1}$.

4.2 Stellar mass

Fitting the spectral energy distribution (SED) of a galaxy is one of the most commonly used methods to determine its stellar mass (e.g. Cid Fernandes et al. 2005; Asari et al. 2007). The advantage of this method is that it can be applied to galaxies at any redshift and can separate stellar from nebular emission. Here we derive the stellar mass of J0811+4730 from fitting the SEDs of both its SDSS and LBT spectra.

Given the data at hand, it is the only method we can use. The equivalent width of the $H\beta$ emission line in both spectra of J0811+4730 is high, $EW(H\beta) \sim 280 \text{ \AA}$, indicating that star formation occurs in a burst and that the contribution of the nebular continuum is also high and should be taken into account in the SED fitting, in addition to the stellar emission. In particular, the fraction of the nebular continuum near $H\beta$ is ~ 30 per cent, and it is considerably higher near $H\alpha$. The details of the SED fitting are described e.g. in Izotov, Guseva & Thuan (2011) and Izotov et al. (2015). The salient features are as follows.

We carried out a series of Monte Carlo simulations to reproduce the SED of J0811+4730. To calculate the contribution of the stellar emission to the SEDs, we adopted the grid of the Padua stellar evolution models by Girardi et al. (2000) with heavy element mass fraction $Z = 0.0004$, or 1/50 solar. To reproduce the SED of the stellar component with any star-formation history, we used the STARBURST99 models (Leitherer et al. 1999, 2014) to calculate a grid of instantaneous burst SEDs for a stellar mass of $1 M_\odot$ in a wide range of ages from 0.5 Myr to 15 Gyr, and Lejeune, Buser & Cuisiner (1997) stellar atmosphere models. We adopted a stellar initial mass function with a Salpeter slope (Salpeter 1955), an upper mass limit of $100 M_\odot$, and a lower mass limit of $0.1 M_\odot$. Then the SED with any star-formation history can be obtained by integrating the instantaneous burst SEDs over time with a specified time-varying SFR.

We approximated the star-formation history in J0811+4730 by a recent short burst forming young stars at age $t_y < 10$ Myr and a prior continuous star formation with a constant SFR responsible for the older stars with ages ranging from t_2 to t_1 , where $t_2 > t_1$ and varying between 10 Myr and 15 Gyr. Zero age is now. The contribution of each stellar population to the SED was parameterized by the ratio of the masses of the old to young stellar populations, $b = M_y/M_o$, which we varied between 0.01 and 100.

The total modelled monochromatic (nebular and stellar) continuum flux near the $H\beta$ emission line for a mass of $1 M_\odot$ was scaled to fit the monochromatic extinction- and aperture-corrected luminosity of the galaxy at the same wavelength. The scaling factor is equal to the total stellar mass M_* in solar units. In our fitting model, $M_* = M_y + M_o$, where M_y and M_o were derived using M_* and b .

The SED of the nebular continuum was taken from Aller (1984). It included hydrogen and helium free-bound, free-free, and two-photon emission. In our models, this was always calculated with the electron temperature $T_e(H^+)$ of the H^+ zone, which is not necessarily equal to $T_e(O III)$. We thus vary it in the range $(0.95 - 1.05) \times T_e(O III)$. The fraction of the nebular continuum near $H\beta$ is defined as the ratio of the observed $EW(H\beta)$ to the pure nebular value, which is $\sim 900 - 1000 \text{ \AA}$, depending of the electron temperature. The observed intensities of the emission lines from the LBT spectrum were corrected for reddening and scaled using the flux of the $H\beta$ emission line and were added to the calculated nebular continuum. However, these lines were not used in the SED fitting, because we fit only the continuum. We also varied the extinction coefficient $C(H\beta)_{SED}$ in the range of $(0.9 - 1.1) \times C(H\beta)$, where $C(H\beta) = 0.165$, the extinction coefficient derived from the observed hydrogen Balmer decrement in the LBT spectrum.

Table 4. Parameters of the lowest-metallicity SFGs

Name	12+logO/H	M_B	M_g	O ₃	O ₃₂	R ₂₃	N ₂	Ref.
J0811+4730	6.98±0.02	...	-15.4	1.61	9.65	2.34	0.0023	1
SBS0335-052W#2	7.01±0.07	-14.7	...	1.48	4.91	2.27	...	2
AGC198691	7.02±0.03	...	-11.5	1.28	2.74	2.17	0.0058	3
SBS0335-052E#7	7.12±0.04	-17.3	...	1.94	7.78	2.84	0.0031	2
IZw18NW	7.16±0.01	...	-15.3	1.95	6.83	2.89	0.0034	4
LeoP	7.17±0.04	-8.8	...	1.45	3.12	2.40	0.0091	5
J1220+4915	7.18±0.03	...	-12.8	2.97	13.48	4.19	0.0051	6
IZw18SE	7.19±0.02	...	-15.3	1.60	2.68	2.73	0.0072	4
DDO68	7.20±0.05	-15.8	...	1.89	3.26	2.47	0.0057	7
SBS0335-052W#1	7.22±0.07	-14.7	...	1.30	1.73	2.49	0.0122	2
J2104-0035	7.24±0.02	...	-12.2	2.79	13.95	3.92	0.0025	6
SBS0335-052E#1+2	7.28±0.01	-17.3	...	3.03	13.90	4.27	0.0036	2

Notes. O₃=[O III]λ5007/Hβ, O₃₂=[O III]λ5007/[O II]λ3727, R₂₃=([O II]λ3727+[O III]λ4959+[O III]λ5007)/Hβ, N₂=[N II]λ6584/Hα.

References. 1 - this paper, 2 - Izotov et al. (2009), 3 - Hirschauer et al. (2016), 4 - Izotov & Thuan (1998), 5 - Skillman et al. (2013), 6 - Izotov et al., in preparation, 7 - Berg et al. (2012).

For J0811+4730, we calculated 5×10^5 Monte Carlo models for each of the SDSS and LBT spectra by varying t_y , t_1 , t_2 , b , and $C(H\beta)_{\text{SED}}$. The best model should satisfy three conditions. First, the modelled EW(Hβ) should match the observed value, within the adopted range between 0.95 and 1.05 times its nominal value. Second, the modelled EW(Hα) should also match the observed value, in the same range between 0.95 and 1.05 times its nominal value. As compared to our previous work, this condition is introduced here for the first time as it would better constrain the models. Third, among the models satisfying the first and the second conditions, the best modelled SEDs of the SDSS and LBT spectra were found from χ^2 minimization of the deviation between the modelled and the observed continuum at ten wavelength ranges, which are selected to cover the entire spectrum and to be free of emission lines and residuals of night sky lines.

From the fit of the SDSS spectrum, we find that the best model for the stellar population consists of young stars with an age $t_y = 3.28$ Myr and a stellar mass $M_y = 10^{6.13} M_\odot$, and of older stars formed continuously with a constant SFR over the time period from 770 Myr to 930 Myr and a stellar mass $M_o = 10^{5.59} M_\odot$, or 3.5 times lower than the stellar mass of the young stellar population. Correspondingly, the total stellar mass of the galaxy is $M_\star = M_y + M_o = 10^{6.24 \pm 0.33} M_\odot$. This implies that 78% of the total stellar mass has been formed during the most recent burst of star formation. Similarly, from the fit of the LBT spectrum, we derive $M_y = 10^{6.18} M_\odot$ for the young population with an age $t_y = 3.28$ Myr, and a mass $M_o = 10^{5.63} M_\odot$ of older stars formed continuously with a constant SFR over the time period from 100 Myr to 290 Myr. This corresponds to a total stellar mass $M_\star = 10^{6.29 \pm 0.06} M_\odot$, in agreement, within the errors, with the value obtained from fitting the SDSS spectrum. All masses obtained from the SDSS spectrum have been corrected for aperture effects using the SDSS g -band total magnitude and the g magnitude inside the 2 arcsec SDSS aperture. This correction would be somewhat different for the LBT spectrum obtained with a 1.2 arcsec wide slit. We do not have enough data to determine the LBT aperture correction accurately, so for the sake of simplicity, we have adopted the same aperture correction for the LBT

data as for the SDSS data. The good agreement between the SDSS and LBT stellar masses suggests that this procedure is not too far off.

We note that the determination of the age and the mass of the old stellar population is somewhat uncertain because its contribution to the continuum in the optical range is low, not exceeding 6 per cent near Hβ and 7 per cent near Hα in the best model. However, even if we fix the formation period of the old stellar population to be between 1 Gyr and 10 Gyr ago, i.e. we assume the least luminous old stellar population with the highest mass-to-luminosity ratio, we still find from SED fitting a small total stellar mass $M_\star \sim 10^{6.34} M_\odot$. Moreover, setting additionally $C(H\beta) = 0$ in the SED fitting does not change the conclusion about the low galaxy stellar mass.

The rest-frame extinction-corrected SDSS and LBT spectra overlaid by the SEDs of the best models are shown in Fig. 2a and 2b, respectively. The nebular, stellar and total (nebular plus stellar) SEDs are shown respectively by thin solid, dashed and thick solid lines. We use only regions clean of galaxy emission lines and night-sky residuals to fit the SEDs. They are shown in Fig. 2 by short horizontal lines.

We find that the contribution of the nebular continuum near the Hβ emission line is nearly 32 per cent of the total continuum emission in that region. Furthermore, the SED of the nebular continuum is shallower than the stellar continuum SED (compare the thin solid and dashed lines in Fig. 2). This makes the fraction of nebular continuum increase to ~50 per cent of the total near the Hα emission line. Therefore, neglecting the nebular continuum, i.e. assuming that the continuum shown by the thick solid line in Fig. 2 is purely stellar in origin, would result in an older stellar population and a larger stellar mass. Indeed, with this assumption, we find a stellar mass which is 0.56 dex higher than the one derived above. This overestimate of the stellar mass is consistent with the finding of Izotov et al. (2011) who compared the stellar mass determinations for similar compact SFGs, dubbed "Green Peas", with the method described in this paper and the method used by Cardamone et al. (2009), which does not take into account nebular continuum emission. Izotov et al. (2011) found that the neglect of the nebular continuum contribution would result in an overestimate

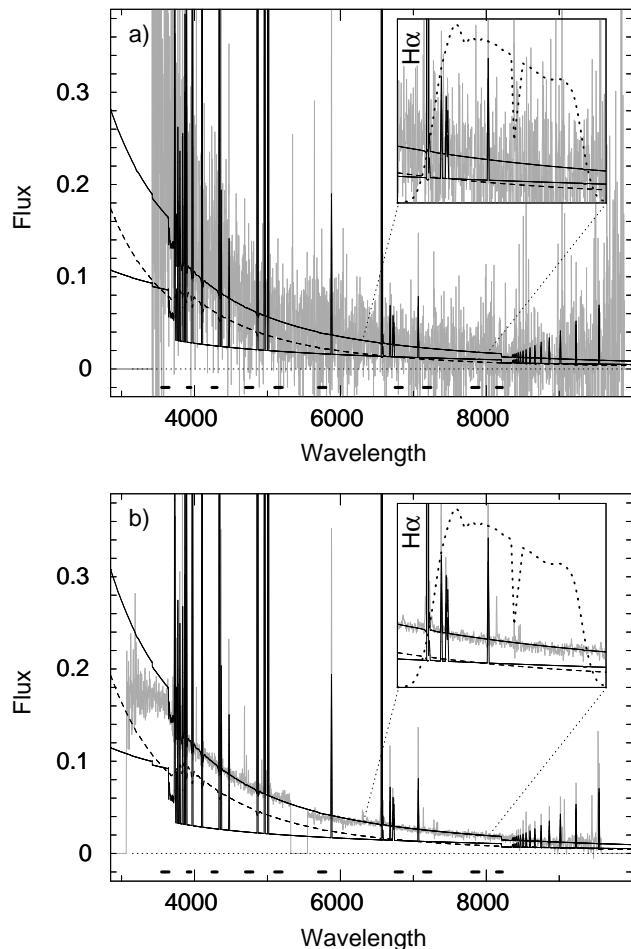


Figure 2. **a)** The rest-frame extinction-corrected SDSS spectrum of J0811+4730 overlaid by the modelled nebular SED (thin solid line), stellar SED (dashed line), and total (stellar and nebular) SED (thick solid line). Short horizontal lines indicate wavelength ranges used for SED fitting. The inset shows the expanded part of the spectrum that falls into the SDSS *i* photometric band. The dotted line in the inset is the transmission curve of the SDSS *i* filter. Wavelengths are in Å and fluxes are in units of 10^{-16} erg s^{-1} cm^{-2} Å $^{-1}$. **b)** Same as in **a)**, but the rest-frame extinction-corrected LBT spectrum of J0811+4730 and SED fits to it are shown. The meaning of the lines is the same as in **a)**.

of the stellar masses of compact SFGs with $EW(H\beta) \geq 100\text{Å}$ by 0.4 dex on average.

In principle, the stellar mass of the old stellar population in galaxies can be estimated from the SDSS *i* magnitude, if all light in this band is stellar and assuming a value for the mass-to-light ratio which for the oldest stars is ~ 1 , if the mass and luminosity are expressed in solar units. However, this technique does not work for J0811+4730 because the contribution of the cool and old stars to its *i*-band luminosity is small. To demonstrate this, we show in insets of Fig. 2 the parts of the spectra that fall into the SDSS *i*-band, with the dotted lines representing the *i*-band transmission curve, with a full passband width FWHM $\sim 1200\text{Å}$. It is seen that the $H\alpha$ emission line, with a $EW(H\alpha)$ of $\sim 1700\text{Å}$, is redshifted to a wavelength where the sensitivity of the transmission curve is still $\sim 1/3$ of its maximum value. Therefore, the $H\alpha$ line contributes, within the spectroscopic

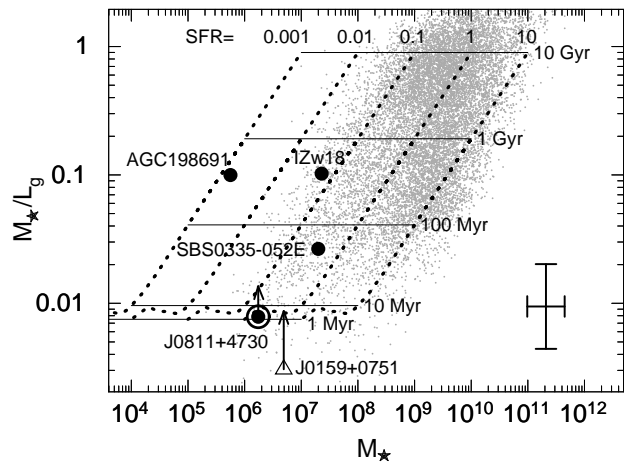


Figure 3. Relation between the stellar mass-to-luminosity ratio and the stellar mass. All quantities are corrected for spectroscopic aperture and extinction, and are expressed in solar units. Selected lowest-metallicity SFGs with $12+\log O/H < 7.3$ are represented by labelled filled circles. The galaxy J0811+4730 is encircled. The error bar indicates the errors of M_* and M_*/L_g for this SFG. By an open triangle is shown the SFG J0159+0751, characterized by very high $O_{32} = [O\ III]\lambda 5007/[O\ II]\lambda 3727 = 39$ and $EW(H\beta) = 347\text{Å}$ (Izotov, Thuan & Guseva 2017). Arrows indicate the upward shifts of the latter SFG and J0811+4730 if the contribution of the $H\beta$ and $[O\ III]\lambda 4959, \lambda 5007$ emission in the SDSS *g*-band is excluded. For comparison, are also shown compact SFGs from the SDSS DR12 with redshifts $z > 0.01$ (grey dots, Izotov et al. 2016). Dotted lines represent STARBURST99 models with continuous star formation and a SFR varying from 0.001 to $10 M_{\odot} yr^{-1}$, during the periods from the present to 10 Gyr, 1 Gyr, 100 Myr, 10 Myr, and 1 Myr in the past (horizontal solid lines). These models include the contribution of both the stellar and nebular continua, but not of nebular emission lines.

aperture, $1/3 \times EW(H\alpha) / (1/3 \times EW(H\alpha) + FWHM) \sim 1/3$ of the light in the *i*-band. Furthermore, to account for the high value of $EW(H\alpha)$, about half of the remaining light must be due to the nebular continuum (compare the dashed and thin solid lines in the insets of Fig. 2). This nebular continuum comes from hydrogen recombination and free-free emission and cannot be neglected. We estimate that only $\sim 1/3$ of the J0811+4730 light in the *i*-band is of stellar origin. Furthermore, a major fraction of this stellar emission comes from the Rayleigh-Jeans tail of the radiation distribution of hot and luminous young stars. We thus conclude that only a small fraction of the *i*-band light comes from the old stellar population and that photometry cannot be used for simple mass estimates of the old stellar population in J0811+4730. Only SED fitting of spectra, which includes both the stellar and nebular emission in a wide range of wavelengths, can give physically justified estimates.

The low stellar mass M_* , in addition to its faint absolute magnitude, characterizes J0811+4730 as a dwarf SFG.

4.3 Comparison with I Zw 18

We test the robustness of our method of stellar mass determination by applying it to another extremely metal-poor SFG, I Zw 18. This SFG has been selected because its stellar mass can be determined by at least another indepen-

dent method. Annibali et al. (2013) have used the CMD of its resolved stellar populations to derive a stellar mass of $>10^{7.24} M_{\odot}$ of its main body, adopting a distance of 18.2 Mpc (Aloisi et al. 2007).

This is to be compared with the stellar mass obtained from the SED fitting described above. We use the SDSS spectra of the two brightest NW and SE components constituting the main body of I Zw 18. We obtain aperture-corrected stellar masses $10^{7.34} M_{\odot}$ and $10^{6.30} M_{\odot}$ for the NW and SE components, respectively. The total stellar mass of the I Zw 18 main body derived by SED fitting is therefore $10^{7.38} M_{\odot}$, consistent with the lower limit derived by Annibali et al. (2013) from the CMD.

4.4 Mass-to-luminosity ratio

In Fig. 3 we show the stellar mass-to-luminosity ratio vs. stellar mass diagram for some of the most metal-poor SFGs known (filled circles). The galaxy J0811+4730 is encircled. For three SFGs (J0811+4730, AGC 198691 and I Zw 18), we use SDSS g -band luminosities calculated from the modelled total apparent magnitudes and adopting the absolute g -band magnitude of 5.45 mag for the Sun (Blanton et al. 2003). We note that the total magnitude used for I Zw 18 includes both the SE and NW components. The photometric data for SBS 0335–052E are not present in the SDSS data base. We have therefore adopted for it the B magnitude given by Pustilnik, Pramskij & Kniazev (2004), taking the absolute B magnitude of the Sun to be 5.48 (Binney & Merrifield 1998). We have used the stellar masses of AGC 198691 and SBS 0335–052E derived by Hirschauer et al. (2016) and Izotov et al. (2014), respectively. The stellar masses of I Zw 18 and of J0811+4730 are derived in this paper by SED fitting of their SDSS spectra.

The mass-to-luminosity ratio of J0811+4730 is extremely low, $\sim 1/100$, as derived from both the SDSS and LBT SEDs, or approximately one order of magnitude lower than the mass-to-luminosity ratio of the second most metal-poor galaxy known, SFG AGC 198691 (Hirschauer et al. 2016), and of I Zw 18 (Fig. 3), but only a factor of 3 lower than that of another extremely metal-deficient SFG, SBS 0335–052E. For comparison, we show also in Fig. 3 by grey dots the compact SFGs in the SDSS DR12 (Izotov et al. 2016). The stellar masses for these galaxies are derived from the SEDs, using the same technique as described above. It is evident that, compared to J0811+4730, the majority of the compact SFGs in the SDSS DR12 are characterised by much higher M_{\star}/L_g ratios. However, there is a small, but non-negligible number of SFGs with mass-to-luminosity ratios similar to that of J0811+4730. They are characterized by high equivalent widths $\text{EW}(\text{H}\beta)$ ($> 200\text{\AA}$), as derived from their SDSS spectra.

To study and compare the evolutionary status of compact SFGs, we present in Fig. 3 STARBURST99 continuous star formation models with a constant SFR, occurring from a specified time t in the past to the present. For the sake of definiteness, models have been calculated for a metallicity of 1/20 solar. They are shown by dotted lines, labelled by their SFRs which vary from 0.001 to $10 M_{\odot} \text{ yr}^{-1}$. We indicate by horizontal solid lines the M_{\star}/L_g ratios corresponding to $t = 1 \text{ Myr}$, 10 Myr , 100 Myr , 1 Gyr and 10 Gyr . The behavior of models for other metallicities is similar to that represented

in Fig. 3. It is seen in the Figure that for $t \leq 10 \text{ Myr}$, corresponding to a burst model, the M_{\star}/L_g ratio is very low, ~ 0.01 , and nearly constant, with a value consistent with the one for an instantaneous burst (Leitherer et al. 1999). For larger t , the M_{\star}/L_g ratio increases with stellar mass, following the relation $\sim M_{\star}^{2/3}$, with a corresponding increase of the mass fraction of old stars, approximately following the relation $[M_{\star}(t) - M_{\star}(\leq 10 \text{ Myr})]/M_{\star}(t)$. It is interesting to note that the distribution of compact SFGs from the SDSS DR12 (grey dots in Fig. 3) follows these relations, with an increasing mass fraction of stars with age $> 10 \text{ Myr}$ in more massive compact SFGs, in agreement with the conclusion of Izotov et al. (2011).

According to our SED fitting, a considerable fraction of the stellar mass in J0811+4730 was created during the last burst of star formation. As for the other very metal-poor SFGs shown in Fig. 3, the mass fraction of older stars is higher. According to the locations of I Zw 18, SBS 0335–052E and AGC 198691 in this diagram, older stars with age $> 10 \text{ Myr}$ dominate the stellar mass in those galaxies.

The models in Fig. 3 include both the stellar and nebular continua. However, we note the important contribution of the $\text{H}\beta$ and $[\text{O III}]\lambda 4959$, $\lambda 5007$ emission lines to L_g in SFGs with a very high $\text{EW}(\text{H}\beta)$. Therefore, to compare the M_{\star}/L_g of those SFGs with model predictions, the contribution of the emission lines should be subtracted from the L_g 's derived from their g -band magnitudes. The magnitude of the effect depends on the $\text{EW}(\text{H}\beta)$ and the metallicity. To demonstrate this, we show in Fig. 3 by an open triangle the location of the compact SFG J0159+0751 with a M_{\star}/L_g ratio far below the model predictions. This SFG, with an oxygen abundance $12+\log\text{O}/\text{H} = 7.55$, is characterised by a very high $[\text{O III}]\lambda 5007/[\text{O II}]\lambda 3727$ flux ratio of 39 and an $\text{EW}(\text{H}\beta) = 347\text{\AA}$, indicative of a very young starburst (Izotov, Thuan & Guseva 2017). However, subtracting the nebular line emission would put J0159+0751 in the region allowed by models (shown by an upward arrow in Fig. 3). Excluding nebular line emission results in a more modest upward shift for J0811+4730, also shown by an arrow. The shift is smaller because of a much lower metallicity and thus a much fainter $[\text{O III}]\lambda 4959$, $\lambda 5007$ emission. For the other most metal-poor SFGs shown in Fig. 3, the contribution of nebular emission lines is even lower because of their considerably lower $\text{EW}(\text{H}\beta)$.

5 EMISSION-LINE DIAGNOSTIC AND METALLICITY-LUMINOSITY DIAGRAMS

Izotov et al. (2012) and Guseva et al. (2017) have demonstrated that the lowest-metallicity SFGs occupy a region in the diagram by Baldwin, Phillips & Terlevich (1981) (hereafter BPT), that is quite different from the location of the main-sequence defined by other nearby SFGs. This fact is clearly shown in Fig. 4a. The data for the lowest-metallicity SFGs in this Figure are presented in Table 4. The references in the Table are for the oxygen abundances. The most metal-deficient SFG known, J0811+4730, is shown as an encircled filled circle in this diagram. It is the most outlying object among the sequence defined by the lowest-metallicity SFGs

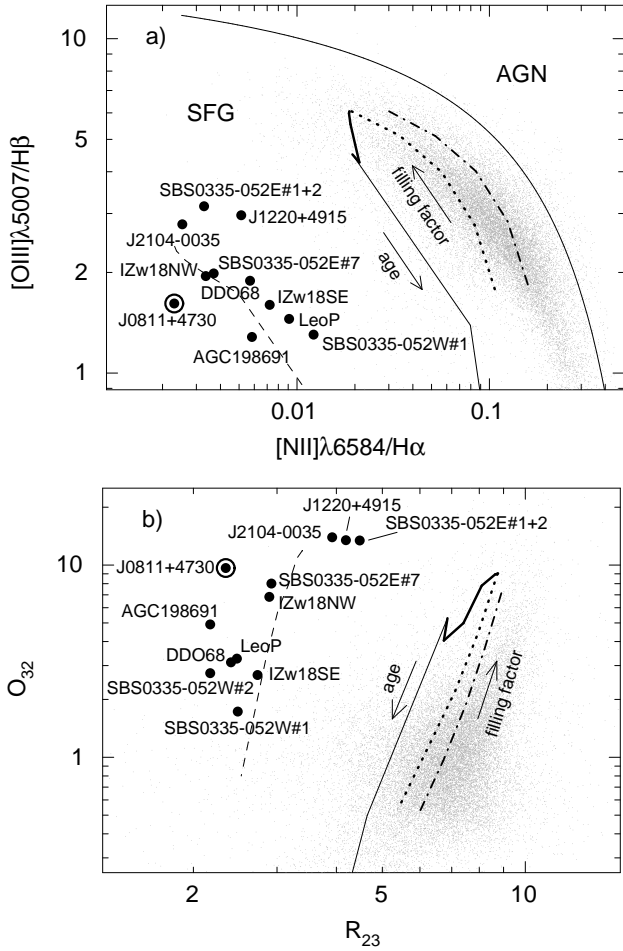


Figure 4. (a) The $[O\ III]\lambda 5007/H\beta - [N\ II]\lambda 6584/H\alpha$ diagnostic diagram (BPT; Baldwin, Phillips & Terlevich 1981). The lowest-metallicity SFGs with $12+\log O/H < 7.3$ are shown by filled circles. The galaxy J0811+4730 is encircled. For comparison, are shown compact SFGs from the SDSS DR12 (grey dots, Izotov et al. 2016). The thin solid line by Kauffmann et al. (2003) separates SFGs from active galactic nuclei (AGN). Dashed and thick solid lines represent relations obtained for CLOUDY photoionized H II region models with $12+\log O/H = 7.3$ and 8.0, respectively, and with different starburst ages ranging from 0 Myr to 6 Myr. Models with $12+\log O/H = 8.0$ and starburst ages of 0 - 4 Myr, corresponding to the highest $H\beta$ luminosity and equivalent width are represented by a thicker solid line. The model dependences with a zero starburst age but with a varying filling factor in the range $10^{-1} - 10^{-3}$, for two oxygen abundances $12+\log O/H = 8.0$ and 8.3, are shown by dotted line and dash-dotted line, respectively. The directions of increasing age and filling factor are indicated respectively by downward and upward arrows. (b) The $O_{32} - R_{23}$ diagram for SFGs, where $O_{32} = [O\ III]\lambda 5007/[O\ II]\lambda 3727$ and $R_{23} = ([O\ II]\lambda 3727 + [O\ III]\lambda 4959 + [O\ III]\lambda 5007)/H\beta$. The meaning of lines and symbols is the same as in (a).

(filled circles) which is itself much shifted to the left from the “normal” SFG main-sequence (grey dots).

The shift of the sequence to the left of the BPT diagram is caused by lower metallicities. To demonstrate this, we plot the $[O\ III]\lambda 5007/H\beta - [N\ II]\lambda 6584/H\alpha$ relations as derived from photoionization H II region models for two oxygen abundances, $12+\log O/H = 7.3$ (dashed line) and 8.0 (solid line), and for various ages of the starburst, ranging

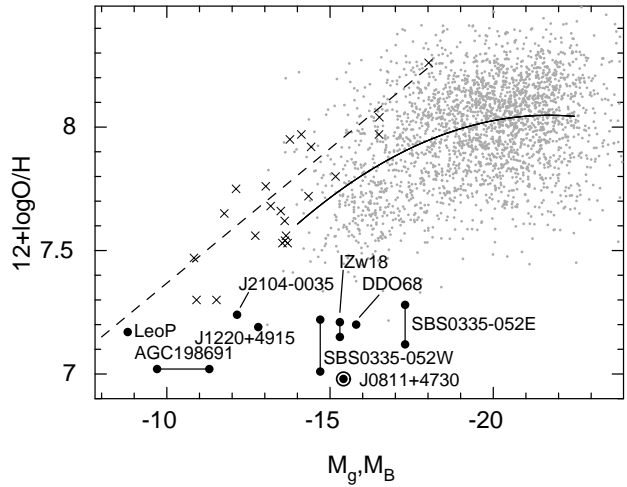


Figure 5. The oxygen abundance - absolute magnitude diagram. Low-luminosity galaxies (crosses), with the fit to these data by Berg et al. (2012) (dashed line). The solid line is the fit to the SDSS compact SFGs from DR12 with oxygen abundances derived by the direct T_e method (grey dots, Izotov et al. 2016). Other symbols are the same as in Fig. 4. Vertical solid lines indicate the ranges of oxygen abundance in different star-forming regions in I Zw 18, SBS 0335-052W and SBS 0335-052E. Horizontal line connects the positions of AGC 198691, calculated with two distances, 8 and 16 Mpc.

from 0 to 6 Myr. The direction of age increase is indicated by the downward arrow. The models are calculated with the CLOUDY code c13.04 (Ferland et al. 1998, 2013), adopting a production rate of ionizing radiation $Q = 10^{53} \text{ s}^{-1}$ and a filling factor $f = 10^{-1}$. Since the location of the theoretical relations depends on the adopted input N/O abundance ratio, we have adopted $\log N/O = -1.5$ for models with $12+\log O/H = 7.3$, and $\log N/O = -1.2$ for models with $12+\log O/H = 8.0$, values that are typical of low-metallicity SFGs (e.g. Izotov et al. 2006). The part of the modelled dependence with $12+\log O/H = 8.0$ and starburst ages 0 - 4 Myr, corresponding to the stages with highest $H\beta$ luminosities and equivalent widths, is shown by a thicker solid line. Izotov et al. (2016) selected the SDSS DR12 compact SFGs (grey dots) to have high $EW(H\beta)$ and thus they correspond to this part of the modelled sequence.

We note however that the location of the modelled sequences in Fig. 4 depends on the adopted input parameters and therefore they are shown only to illustrate dependences on metallicities. The location of main-sequence SFGs is closest to models with oxygen abundance $12+\log O/H = 8.0$. For comparison, we also show the modelled dependences with a fixed starburst age of 0 Myr, but varying the filling factor in the range $10^{-1} - 10^{-3}$ for oxygen abundances $12 + \log O/H = 8.0$ (dotted line) and 8.3 (dash-dotted line). The effect of an increasing filling factor is shown by an upward arrow. These models reproduce much better the location of the main-sequence SFGs (grey dots). This is to be expected since Izotov et al. (2016) selected from the SDSS DR12 only compact SFGs with high $EW(H\beta)$, as noted above, i.e. with young bursts. On the other hand, the location of the lowest-metallicity SFGs agrees well with models calculated for an oxygen abundance $12+\log O/H = 7.3$.

Similarly, the lowest-metallicity SFGs are located in the

$O_{32} - R_{23}$ diagram in a region which is very different from that of the main-sequence of the SDSS SFGs (Fig. 4b), with J0811+4730 being one of the galaxies most shifted to the left (encircled filled circle). These shifts to the left are again primarily due to lower metallicities. This is seen by comparing the predictions of models with varying starburst age for $12+\log O/H = 7.3$ (dashed line) and 8.0 (solid line). It is also seen that models for zero-age starbursts with varying filling factors for $12+\log O/H = 8.0$ (dotted line) and 8.3 (dash-dotted line) reproduce much better the location of the main-sequence galaxies (grey dots) as compared to the modelled sequence of bursts with a varying age (solid line).

We emphasize that the modelled emission-line ratios in Fig. 4 have been calculated taking into account only stellar ionizing radiation. These ratios may be changed if additional sources of ionization and heating such as shocks and X-ray emission are present. Inclusion of these additional sources would enhance the $[O\ II]\lambda 3727$ emission line relative to the $[O\ III]\lambda 5007$ emission line (e.g. Stasińska et al. 2015), reducing O_{32} and shifting the modelled sequences downward.

Finally, in Fig. 5 we present the oxygen abundance – absolute magnitude relation for SFGs. For some galaxies, absolute B -band magnitudes have been adopted, while for others absolute SDSS g -band magnitudes have been used. This difference in the adopted magnitudes will change little the distributions of SFGs in Fig. 5 because the differences in g and B magnitudes for SFGs are small, $\lesssim 0.1$ mag. We also note that M_B for AGC 198691 in Table 4 is derived assuming a distance of 16 Mpc.

Oxygen abundances for all galaxies shown in this Figure have been derived by the direct T_e method. In particular, only compact SFGs from the SDSS DR12 (grey dots) with an $[O\ III]\lambda 4363$ emission line detected in their spectra with an accuracy better than 50 per cent, allowing a reasonably good determination of $12+\log O/H$ by the direct method, are included. Following Izotov et al. (2015), we stress the importance of using the same method of metallicity determination for all data, to exclude biases introduced by different methods and to produce an homogeneous set of data. In particular, Izotov et al. (2015) showed that, concerning the often cited oxygen abundance – absolute magnitude and oxygen abundance – stellar mass relations derived for SFGs by Tremonti et al. (2004), the metallicities derived by strong-line methods can be by as much as 0.5 dex higher compared to the metallicities derived by the direct method for the same SFGs. They are inconsistent with those derived by other strong-line methods such as those proposed e.g. by Pettini & Pagel (2004), Pilyugin & Thuan (2005) and Izotov et al. (2015). Those authors calibrated their relations using oxygen abundances derived by the direct method, and the abundances obtained from their calibrations are thus consistent with the T_e method.

The lowest-metallicity SFGs present a wide range of absolute magnitudes. The two galaxies with the lowest luminosities are Leo P (Skillman et al. 2013) and AGC 198691 (Hirschauer et al. 2016). The first galaxy follows well the relation found by Berg et al. (2012) for relatively quiescent SFGs, while the second one deviates somewhat from it to a higher luminosity.

On the other hand, some other lowest-metallicity SFGs, including J0811+4730, strongly deviate from the Berg et al.

(2012) relation. Izotov et al. (2012) and Guseva et al. (2017) have attributed these deviations to the enhanced brightnesses of the galaxies undergoing active star formation. In particular, we estimate that the luminosity increase for J0811+4730 with its high $EW(H\beta)$ would be as much as 2 magnitudes, due to the contribution of the nebular continuum and emission lines to the g -band luminosity. However, such an increase is insufficient to explain the whole deviation.

Additionally, these galaxies can also be chemically unevolved objects with a short star formation history, having too low metallicities for their high luminosities. Indeed, star formation in a system such as SBS 0335–052E is very different from that in dwarfs like Leo P and AGC 198691. It is currently undergoing a powerful burst, giving birth to bright low-metallicity super-star clusters containing thousands of massive O-stars (Thuan, Izotov & Lipovetsky 1997), followed by a delayed element enrichment. A similar scenario can be at work in J0811+4730 and at high redshifts, in zero-metallicity dwarf primeval galaxies, undergoing their first burst of star formation.

Finally, Ekta & Chengalur (2010) have proposed to explain these low metallicities by the infall of gas from galactic halos. The effective mixing of the metal-poor gas in the halos with the more metal-rich gas in the central part of the galaxies will dilute the latter, decreasing its metallicity. Clearly more observational and modelling work is needed to understand the true nature of J0811+4730.

6 CONCLUSIONS

In this paper we present Large Binocular Telescope (LBT) spectrophotometric observations of the compact star-forming galaxy (SFG) J0811+4730 selected from the Data Release 13 (DR13) of the Sloan Digital Sky Survey (SDSS). We find that the oxygen abundance of this galaxy is $12+\log O/H = 6.98 \pm 0.02$, the lowest ever found for a nearby SFG, and the first one below $12+\log O/H = 7.0$. J0811+4730 strongly deviates from the SDSS main-sequence SFGs in the $[O\ III]\lambda 5007/H\beta - [N\ II]\lambda 6584/H\alpha$ and $[O\ III]\lambda 5007/[O\ II]\lambda 3727 - ([O\ II]\lambda 3727 + [O\ III]\lambda 4959 + [O\ III]\lambda 5007)/H\beta$ diagrams because of its extremely low metallicity. In the same way as other galaxies with very low metallicities, it is also strongly offset in the oxygen abundance – absolute magnitude diagram from the relations defined by nearby galaxies (Berg et al. 2012) and compact SFGs (Izotov et al. 2016). This offset can probably be explained by a combination of its chemically unevolved nature, an enhanced brightness of its star-forming regions, and gas infall resulting in the dilution of the more metal-rich gas in the inner region by the outer more metal-poor gas in the halo.

The properties of the local lowest-metallicity SFGs are likely close to those of the high-redshift low-luminosity SFGs recently found at $z > 3$ (Karman et al. 2017), and thought to have played an important role in the reionization of the Universe at $z > 5$ (Ouchi et al. 2009).

ACKNOWLEDGEMENTS

We thank D. M. Terndrup and C. Wiens for help with the LBT observations. We are grateful to anonymous referees for useful comments on the manuscript. Funding for the Sloan Digital Sky Survey IV has been provided by the Alfred P. Sloan Foundation, the U.S. Department of Energy Office of Science, and the Participating Institutions. SDSS-IV acknowledges support and resources from the Center for High-Performance Computing at the University of Utah. The SDSS web site is www.sdss.org. SDSS-IV is managed by the Astrophysical Research Consortium for the Participating Institutions of the SDSS Collaboration. This research has made use of the NASA/IPAC Extragalactic Database (NED), which is operated by the Jet Propulsion Laboratory, California Institute of Technology, under contract with the National Aeronautics and Space Administration.

REFERENCES

- Albaret F. D. et al., 2016, *ApJS*, in press; preprint arXiv:1608.02013
- Aller L. H., 1984, *Physics of Thermal Gaseous Nebulae* (Dordrecht: Reidel)
- Aloisi A. et al., 2007, *ApJ*, 667, L151
- Annibali F. et al., 2013, *AJ*, 146, 144
- Asari N. V., Cid Fernandes R., Stasińska G., Torres-Papaqui J. P., Mateus A., Sodré L. Jr., Schoenell W., Gomes J. M., 2007, *MNRAS*, 381, 263
- Baldwin J. A., Phillips M. M., Terlevich R., 1981, *PASP*, 93, 5
- Berg D. A. et al., 2012, *ApJ*, 754, 98
- Binney J., Merrifield M., 1998, *Galactic Astronomy* (Princeton University Press)
- Blanton M. R. et al., 2003, *ApJ*, 592, 819
- Cardamone C. et al., 2009, *MNRAS*, 399, 1191
- Cardelli J. A., Clayton G. C., Mathis J. S., 1989, *ApJ*, 345, 245
- Chávez R., Terlevich E., Terlevich R., Plionis M., Bresolin F., Basilakos S., Melnick J., 2012, *MNRAS*, 425, L56
- Cid Fernandes R., Mateus A., Sodré L. Jr., Stasińska G., Gomes J. M., 2005, *MNRAS*, 358, 363
- Ekta B, Chengalur J. N., 2010, *MNRAS*, 406, 1238
- Ferland G. J., Korista K. T., Verner D. A., Ferguson J. W., Kingdon J. B., Verner E. M., 1998, *PASP*, 110, 761
- Ferland G. J. et al., 2013, *Revista Mexicana de Astronomía y Astrofísica*, 49, 137
- Filippenko A. V., 1982, *PASP*, 94, 715
- Gallazzi A., Bell E. F., 2009, *ApJS*, 185, 253
- Giovanelli R. et al., 2005, *AJ*, 130, 2598
- Girardi L., Bressan A., Bertelli G., Chiosi C., 2000, *A&AS*, 141, 371
- Guseva N. G., Izotov Y. I., Fricke K. J., Henkel C., 2017, *A&A*, 599, A65
- Haynes M. P. et al., 2011, *AJ*, 142, 170
- Hirschauer A. S. et al., 2016, *ApJ*, 822, 108
- Izotov Y. I., Thuan T. X., 1998, *ApJ*, 497, 227
- Izotov Y. I., Thuan T. X., Lipovetsky V. A., 1994, *ApJ*, 435, 647
- Izotov Y. I., Thuan T. X., Guseva N. G., 2005, *ApJ*, 632, 210
- Izotov Y. I., Stasińska G., Meynet G., Guseva N. G., Thuan T. X., 2006, *A&A*, 448, 955
- Izotov Y. I., Guseva N. G., Fricke K. J., Papaderos P., 2009, *A&A*, 503, 61
- Izotov Y. I., Guseva N. G., Thuan T. X., 2011, *ApJ*, 728, 161
- Izotov Y. I., Thuan T. X., Guseva N. G., 2012, *A&A*, 546, 122
- Izotov Y. I., Guseva N. G., Fricke K. J., Krügel E., Henkel C., 2014, *A&A*, 570, A97
- Izotov Y. I., Guseva N. G., Fricke K. J., Henkel C., 2015, *MNRAS*, 451, 2251
- Izotov Y. I., Guseva N. G., Fricke K. J., Henkel C., 2016, *MNRAS*, 462, 4427
- Izotov Y. I., Thuan T. X., Guseva N. G., 2017, *MNRAS*, 471, 548
- Karman W. et al., 2016, *A&A*, 599, A28
- Kauffmann G. et al., 2003, *MNRAS*, 341, 33
- Kennicutt R. C., Jr., 1998, *Ann.Rev.Astron.Astrophys.*, 36, 189
- Law D. R. et al., 2011, *AJ*, 152, 83
- Leitherer C. et al., 1999, *ApJS*, 123, 3
- Leitherer C., Ekström S., Meynet G., Schaerer D., Agienko K. B., Levesque E. M., 2014, *ApJS*, 212, 14
- Lejeune T., Buser R., Cuisinier F., 1997, *A&AS*, 125, 229
- Ouchi M. et al., 2009, *ApJ*, 706, 1136
- Pettini M., Pagel B. E. J., 2004, *MNRAS*, 348, L59
- Pilyugin L., Thuan T.X., 2005, *ApJ*, 631, 231
- Planck Collaboration XVI, 2014, *A&A*, 571, A16
- Pustilnik S. A., Pramskij A. G., Kniazev A. Y., 2004, *A&A*, 425, 51
- Pustilnik S. A., Kniazev A. Y., Pramskij A. G., 2005, *A&A*, 443, 91
- Rudolf N., Günther H. M., Schneider P.C., and Schmitt J. H. M. M., 2016, *A&A*, 585, 113
- Salpeter E. E., 1955, *ApJ*, 121, 161
- Searle L., Sargent W. L. W., 1972, *ApJ*, 173, 25
- Skillman E., Kennicutt R. C. Jr., 1993, *ApJ*, 411, 655
- Skillman E. D. et al., 2013, *AJ*, 146, 3
- Stasińska G., Izotov Y., Morisset C., Guseva N., 2015, *A&A*, 576, A83
- Thuan T. X., Izotov Y. I., Lipovetsky V. A., 1997, *ApJ*, 477, 661
- Tremonti C. et al., 2004, *ApJ*, 613, 898
- Wright E. L., 2006, *PASP*, 118, 1711

This paper has been typeset from a $\text{\TeX}/\text{\LaTeX}$ file prepared by the author.